Check for updates

Molecular Beam Epitaxy and Electronic Structure of Atomically Thin Oxyselenide Films

Yan Liang, Yujie Chen, Yuanwei Sun, Shipu Xu, Jinxiong Wu, Congwei Tan, Xiaofeng Xu, Hongtao Yuan, Lexian Yang, Yulin Chen, Peng Gao, Jiandong Guo, and Hailin Peng**

Atomically thin oxychalcogenides have been attracting intensive attention for their fascinating fundamental properties and application prospects. Bi_2O_2Se, a representative of layered oxychalcogenides, has emerged as an air-stable high-mobility 2D semiconductor that holds great promise for next-generation electronics. The preparation and device fabrication of high-quality Bi_2O_2Se crystals down to a few atomic layers remains a great challenge at present. Here, molecular beam epitaxy (MBE) of atomically thin Bi_2O_2Se films down to monolayer on $SrTiO_3$ (001) substrate is achieved by co-evaporating Bi and Se precursors in oxygen atmosphere. The interfacial atomic arrangements of MBE-grown $Bi_2O_2Se/SrTiO_3$ are unambiguously revealed, showing an atomically sharp interface and atom-to-atom alignment. Importantly, the electronic band structures of one-unit-cell (1-UC) thick Bi_2O_2Se films are observed by angle-resolved photoemission spectroscopy (ARPES), showing low effective mass of ≈0.15 m_0 and bandgap of ≈0.8 eV. These results may be constructive to the synthesis of other 2D oxychalcogenides and investigation of novel physical properties.

Thanks to their rich physics and fascinating application prospects, atomically thin metal oxides/chalcogenides (sulfide, selenide, or telluride) and their heterostructures, such as transition metal dichalcogenides (TMDs),[1,2] superconducting β-phase FeSe,[3,4] topological insulator (Bi_2Se_3, Bi_2Te_3),[5,6] and $LaAlO_3/SrTiO_3$,[7,8] have been attracting tremendous interest over decades. Oxychalcogenides, which can be regarded as mixing and bridging chalcogenides and oxides together, reactivate their research booms for the remarkable phenomena such as high carrier mobility,[9] thermoelectricity,[10–12] ferroelectricity,[13] and superconductivity.[14] Bi_2O_2Se, a representative of oxychalcogenides family, emerged as an air-stable high-mobility layered semiconductor, which holds promise for next-generation digital devices and optoelectronics.[2,9,13,15–23] For example, the bulk Bi_2O_2Se crystals show an ultrahigh Hall mobility of ≈280 000 cm^2 V^{-1} s^{-1} at low temperature[9] and robust bandgap (immune to Se vacancies) after cleavage.[17] Nanoplates and thin films of Bi_2O_2Se were successfully prepared by chemical vapor deposition (CVD),[9,15,21,23] displaying excellent switching behavior of I_{on}/I_{off} and high Hall mobility (up to 450 cm^2 V^{-1} s^{-1}) at room temperature. Outstanding optoelectronic properties were recently observed in CVD-grown Bi_2O_2Se nanoplates.[16,18,23–25] The present research is mainly focused on the bulk crystals and few-layer or multiplayer samples due to the challenge to faithfully achieve the growth of atomically thin Bi_2O_2Se films. The atomically thin counterpart down to one-unit-cell (1-UC)

Dr. Y. Liang, Dr. S. Xu, Dr. J. Wu, C. Tan, Prof. P. Gao, Prof. H. Peng
Center for Nanochemistry
Beijing Science and Engineering Centre for Nanocarbons
College of Chemistry and Molecular Engineering
Peking University
Beijing 100871, P. R. China
E-mail: hlpeng@pku.edu.cn

Y. Chen, Prof. L. Yang, Prof. Y. Chen
State Key Laboratory of Low Dimensional Quantum Physics
Department of Physics
Tsinghua University
Beijing 100084, P. R. China

Y. Sun, Prof. P. Gao
Electron Microscopy Laboratory
School of Physics
and International Center for Quantum Materials
Peking University
Beijing 100871, P. R. China

C. Tan
Academy for Advanced Interdisciplinary Studies
Peking University
Beijing 100871, P. R. China

X. Xu, Prof. J. Guo
Beijing National Laboratory for Condensed Matter Physics & Institute of Physics
Chinese Academy of Sciences
Beijing 100190, P. R. China
E-mail: jdguo@iphy.ac.cn

Prof. H. Yuan
National Laboratory of Solid-State Microstructures
College of Engineering and Applied Sciences, and Collaborative Innovation Center of Advanced Microstructures
Nanjing University
Nanjing 210093, P. R. China

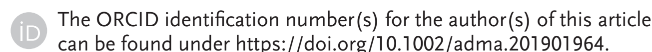
The ORCID identification number(s) for the author(s) of this article can be found under https://doi.org/10.1002/adma.201901964.

DOI: 10.1002/adma.201901964

© 2019 WILEY-VCH Verlag GmbH & Co. KGaA, Weinheim

15214095, 2019, 39, Downloaded from https://onlinelibrary.wiley.com/doi/10.1002/adma.201901964 by Zhejiang University, Wiley Online Library on [04/09/2023]. See the Terms and Conditions (https://onlinelibrary.wiley.com/terms-and-conditions) on Wiley Online Library for rules of use; OA articles are governed by the applicable Creative Commons License

thickness will provide an excellent 2D platform to investigate the physical properties different from bulk one due to quantum size effect. Compared to CVD method, molecular beam epitaxy (MBE), a state-of-the-art technique with ultrahigh vacuum (UHV) environment, has obvious advantages for precise thickness control owing to ultralow growth rate with a 2D growth mode.[26,27] Additionally, the UHV condition ensures the ultraclean surface of the samples, which will facilitate the direct observation of electronic structures of atomically thin films.

Here, for the first time, we exploited the MBE-growth of atomically thin Bi_2O_2Se films down to monolayer (ML) by co-evaporating Bi and Se precursors in oxygen atmosphere. By precisely controlling the growth condition such as flux rates of each components and growth temperature, a 2D growth mode of Bi_2O_2Se was achieved on (001)-oriented $SrTiO_3$ (STO) substrate. Besides, with the assistance of atomically resolved scanning transition electron microscopy (STEM) and energy-dispersive spectroscopy (EDS), the atomic structures at Bi_2O_2Se/STO interface were unambiguously revealed, showing a highly crystalline structure of layered Bi_2O_2Se, atomically sharp interface and atom-to-atom alignment in Bi_2O_2Se/STO. Importantly, the electronic band structures of MBE-grown 1-UC thick Bi_2O_2Se films were successfully revealed by angle-resolved photoemission spectroscopy (ARPES), showing low effective mass of ≈0.15 m_0 and a bandgap of ≈0.8 eV. The very slightly bandgap enlarging of 1-UC Bi_2O_2Se compared to bulk one indicates weak quantum size effects exists in Bi_2O_2Se, which is consistent with the previous generalized gradient approximation (GGA) calculations.[9]

Figure 1a shows the preparation of atomically thin Bi_2O_2Se films by a home-made oxide MBE facility, and more details about film growth are described in the Supporting Information. In our growth, Bi and Se elements are evaporated using standard effusion cells, and oxygen is imported in the chamber through a leakage valve for precisely control the oxygen flow rate. Single polished Nb-doped STO single crystals with excellent conductivity and high thermal stability are chosen as the epitaxial substrates. The utility of Nb-doped STO substrate allows the direct characterization of surface-sensitive tools such as ARPES, where the samples are required to be placed on a conducting substrate. More importantly, as shown in Figure 1b,c, cubic perovskite oxide STO (a = 3.90 Å) provides reasonable lattice matching (≈0.5% mismatch) with Bi_2O_2Se that has a tetragonal crystal structure ($I4/mmm$, a = 3.88 Å, c = 12.16 Å, Z = 2). Before epitaxial growth of Bi_2O_2Se films, the STO (001) substrates are pretreated in UHV at 950 °C for 1 h to obtain single TiO_2-terminated surface.[3] Typical atomic force microscopy (AFM) image of the prepared STO (001) substrate surface shows clear terraces with an identical step height of 0.4 nm (**Figure 2**a), which is consistent with the height of one-unit cell (0.39 nm) of STO (001).

The key to MBE-grown atomically thin Bi_2O_2Se film is the precise control of substrate growth temperature (T_s), Se/Bi flux ratio and oxygen pressure in the MBE system. In detail, we adjust T_s by following the common "three-temperature method," which means T_s is set between the evaporation temperatures of Bi and Se (namely $T_{Bi} > T_s > T_{Se}$). Under the condition of $T_s > T_{Se}$, the residual Se will desorb spontaneously from the surfaces to prevent codeposition or bulk crystal growth.[28] Besides, relatively lower Se/Bi flux (<10) and higher oxygen pressure (>10^{-5} mbar) will suppress the formation of Bi_2Se_3 impurities, and pure Bi_2O_2Se phase will be obtained.[29–32] In our case, the pure Bi_2O_2Se phase can be obtained when Se and Bi flux rates are kept at 7 and 3 Å min^{-1}, respectively, calibrated by quartz crystal microbalance (QCM). It is worth mentioning that there are no other oxygen-rich secondary phases, such as Bi_2O_3 or SeO_2, found in all our attempts to parameter optimization. We found that the optimized MBE growth of atomically thin Bi_2O_2Se occurs at T_s = 290 °C under an oxygen pressure of 1×10^{-4} mbar, since relatively high growth temperature would result in multilayer growth, while relatively low temperature might lead to 3D growth (Figure S1, Supporting Information). As indicated in Figure 2b, at the initial growth stage, monolayer Bi_2O_2Se islands preferentially nucleate along the terraces of STO substrate and form discontinuous 2D islands with irregular edges. With the growth coverage increasing, these isolated monolayer islands merge together and form continuous ML film that covers the STO (001) substrate surface completely and strictly follows the terrace structure (Figure 2c). Monolayer Bi_2O_2Se is defined as half unit cell with the thickness of ≈0.6 nm, which consists of one complete Bi_2O_2 layer plus one complete Se layer.

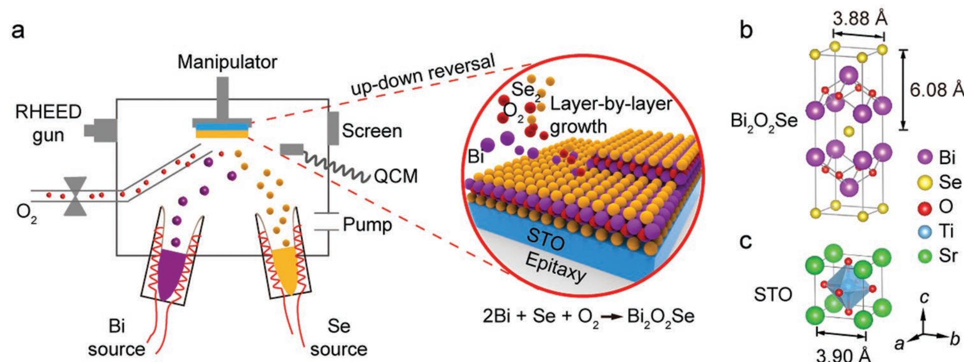

Figure 1. a) Schematic diagram of epitaxial growth of atomically thin Bi_2O_2Se films on a (001)-oriented $SrTiO_3$ (STO) substrate by co-evaporating the Bi and Se precursors in oxygen atmosphere in a home-made MBE setup equipped with reflective high-energy electron diffraction (RHEED) and quartz crystal microbalance (QCM). b,c) Crystal structures of Bi_2O_2Se and STO, respectively, showing negligible lattice mismatch in ab plane and the same in-plane crystal symmetry.

© 2019 WILEY-VCH Verlag GmbH & Co. KGaA, Weinheim

15214095, 2019, 39, Downloaded from https://onlinelibrary.wiley.com/doi/10.1002/adma.201901964 by Zhejiang University, Wiley Online Library on [04/09/2023]. See the Terms and Conditions (https://onlinelibrary.wiley.com/terms-and-conditions) on Wiley Online Library for rules of use; OA articles are governed by the applicable Creative Commons License

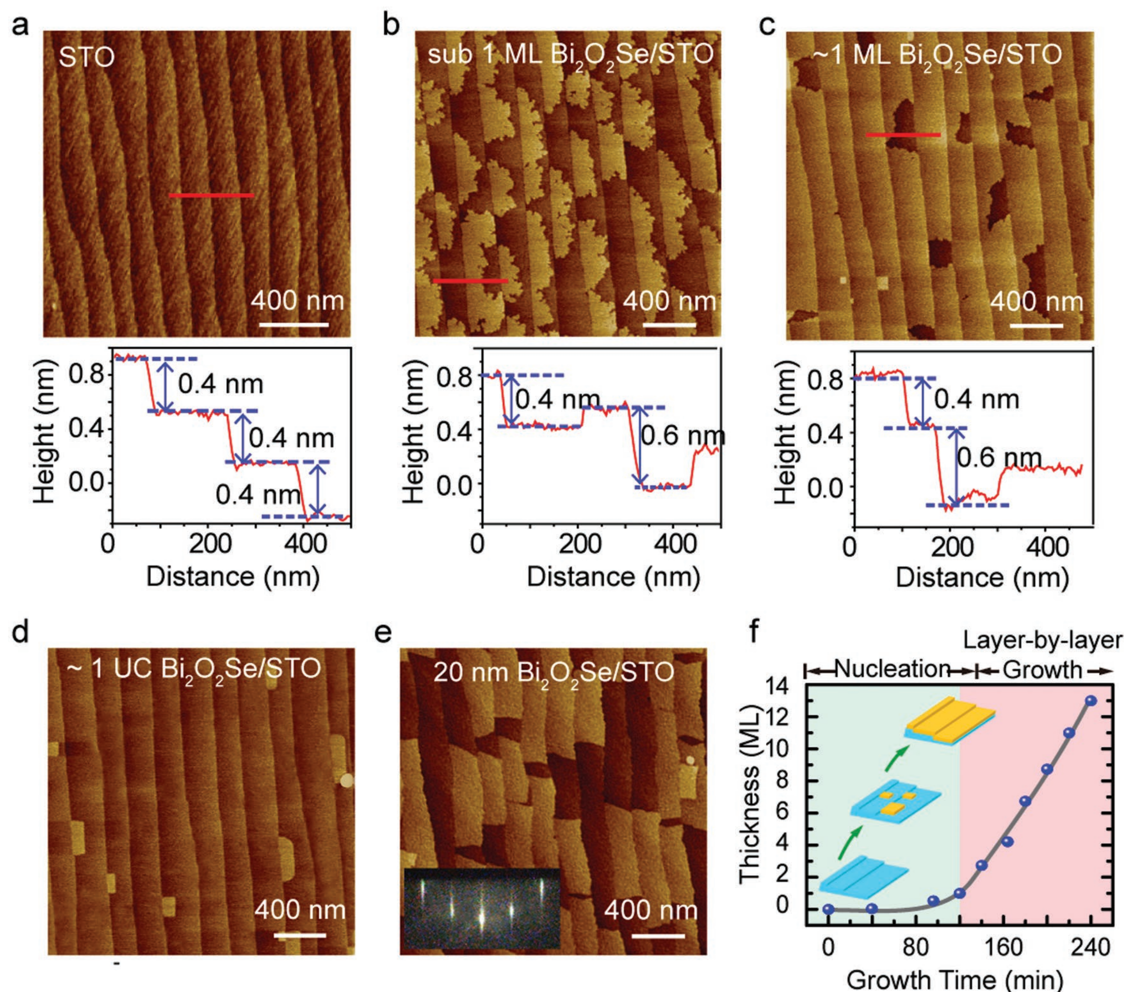

Figure 2. Precise thickness control of Bi_2O_2Se films grown on STO substrate by MBE. a) Surface morphology of TiO_2-terminated STO substrate, showing clear terraces with a step height of 0.4 nm. b–e) AFM topography of MBE-grown Bi_2O_2Se films with variable thicknesses, showing the morphological evolution of Bi_2O_2Se films from: b) the isolated islands nucleated along the terraces of STO substrate, to c) monolayer (1 ML) Bi_2O_2Se film, to d) 1-UC (2 ML) thick Bi_2O_2Se film with new 2D islands formed on the step edges, and to e) 20 nm thick Bi_2O_2Se film. The MBE growth adopts a 2D growth mode, showing clear terrace heights of 0.4 and 0.6 nm originating from STO substrate and Bi_2O_2Se monolayer, respectively. Inset: reflective high-energy electron diffraction (RHEED) pattern of the surface. f) The thickness of MBE-grown Bi_2O_2Se films as a function of growth time, consisting of initial nucleation stage at first ≈100 min and nearly linear growth stage followed.

Further increasing the growth coverage, new 2D Bi_2O_2Se islands with the height of 0.6 nm nucleate at lower terrace edges of the Bi_2O_2Se layer (Figure 2d). Compared with the first layer, the edges of these 2D islands on Bi_2O_2Se layers are regular and parallel to each other, whose orientations register the in-plane lattice direction of STO substrate. The growth of Bi_2O_2Se film maintains the 2D growth mode on STO substrate, until a complete 1-UC thick Bi_2O_2Se film is formed with clear surface step terraces (Figure 2d and Figure S2a, Supporting Information). A thick Bi_2O_2Se film (≈20 nm) can be obtained by extending the growth (Figure 2e and Figure S2b, Supporting Information). Reflective high-energy electron diffraction (RHEED) (inset of Figure 2e) captured in vacuum shows sharp streaky pattern, indicating the existence of smooth and long-range ordered surface. The single crystallinity of the film has been confirmed by low energy electron diffraction (LEED) and X-ray diffraction (XRD) (Figure S3, Supporting Information). It is worth noting that the effective growth rate is nonlinear upon time. Figure 2f illustrates the film thickness as a function of growth time. With fixed growth parameters, the first layer growth spends nearly 2 h, while the growth rate increases to ≈20 min per 1 ML and keeps almost constant for the growth of the following layers. This observation reveals that homoepitaxy of Bi_2O_2Se is favored much more than heteroepitaxy on STO.

To further study elemental compositions and atomic alignment of MBE-grown Bi_2O_2Se/STO interface, we performed the systematic characterization of cross-sectional aberration-corrected STEM on the sample (**Figure 3**). High-angle annular dark-field (HAADF)-STEM images show an atomically sharp interface between Bi_2O_2Se and STO (Figure 3a,b), where strongly bonded heterointerfaces with a strict epitaxial growth are revealed. Additionally, the geometric phase analysis (GPA) is applied on the HAADF image to elucidate whether or not there is interfacial stress in the epitaxial film (Figure 3c,d). The strain

 © 2019 WILEY-VCH Verlag GmbH & Co. KGaA, Weinheim

15214095, 2019, 39, Downloaded from https://onlinelibrary.wiley.com/doi/10.1002/adma.201901964 by Zhejiang University, Wiley Online Library on [04/09/2023]. See the Terms and Conditions (https://onlinelibrary.wiley.com/terms-and-conditions) on Wiley Online Library for rules of use; OA articles are governed by the applicable Creative Commons License

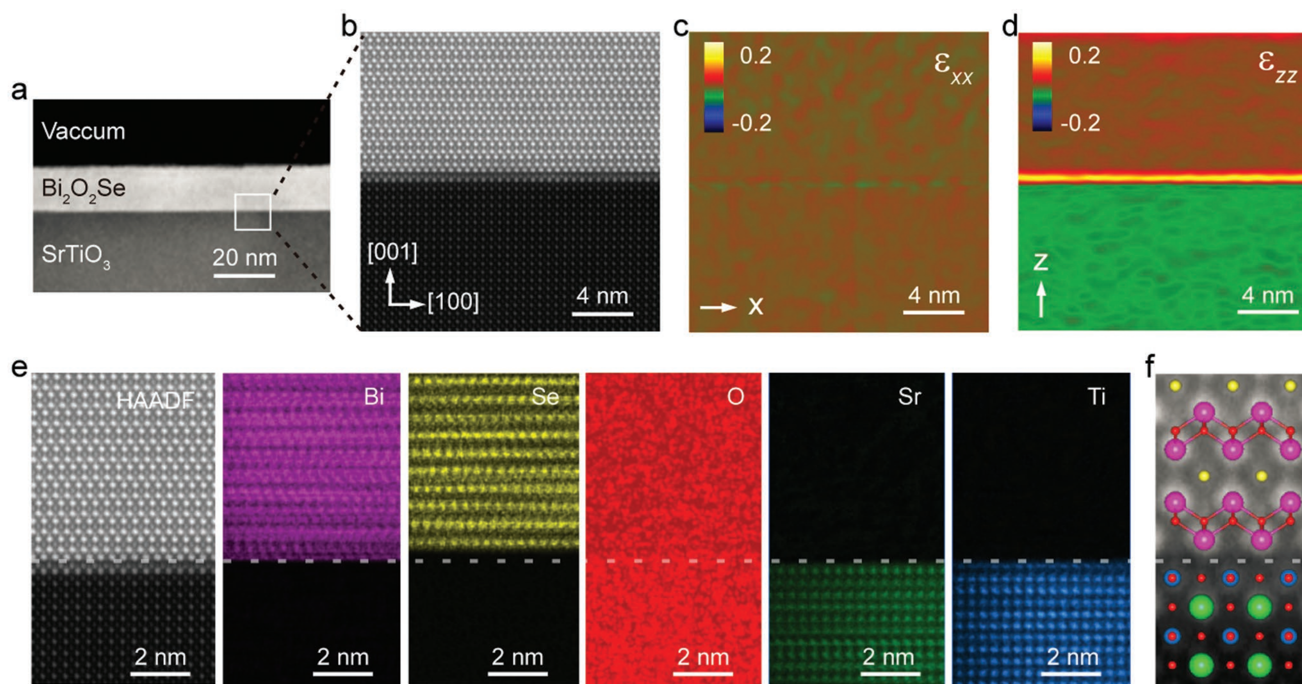

Figure 3. Cross-sectional TEM characterization of MBE-grown Bi_2O_2Se on STO. a) Cross-sectional HAADF-STEM image of the interface between Bi_2O_2Se film (≈20 nm) and STO. b) Atomic-resolution HAADF-STEM image of the interface, corresponding to the white box in (a). c,d) GPA of the HAADF image in (b) with uniaxial strain components ε_{xx} (c) and ε_{zz} (d). All the strain analysis is in reference to the crystal lattice of STO. e) Atomically resolved elemental maps of Bi, Se, O, Sr, and Ti across the interfaces by EDS. f) HAADF-STEM image of the interface with atomic model placed on.

map along x-axis parallel to STO (100) reveals that Bi_2O_2Se film has identical lattice spacing to that of the STO. This observation indicates that the Bi_2O_2Se/STO interface is nearly free of in-plane misfit strains and dislocations, which results from the perfect in-plane lattice match of Bi_2O_2Se/STO. Along the z-axis parallel to STO (001), the lattice spacing is homogenous in the Bi_2O_2Se film while increases significantly in the first layer near the interface, presumably originating from the larger spacing between first layer of Bi_2O_2Se and STO. Atomically resolved EDS is further performed to investigate atomic arrangements at the interface. Figure 3e shows maps for bismuth (Bi), selenium (Se), oxygen (O), strontium (Sr), and titanium (Ti), respectively, which unambiguously unveils the perfect atomic arrangements of the interface. Layered Bi_2O_2Se contains a stacked structure of Bi_2O_2–Se–Bi_2O_2–Se. The Bi atoms of Bi_2O_2Se are clearly aligned with Sr at the interface between the Bi_2O_2Se and the TiO_2-terminated STO (Figure 3f), indicating a perfect epitaxial match.

The 2D epitaxy of high-quality Bi_2O_2Se films on conducting Nb-doped STO via MBE allows direct observation of electronic band structures of atomically thin Bi_2O_2Se by ARPES. The UHV condition during MBE can ensure the clean surface with no contaminations and environmental degradation of the MBE samples. A vacuum suitcase with base pressure lower than 1×10^{-8} mbar was used to keep the film surface fresh during sample transfer process from the MBE chamber to the ARPES system. As shown in **Figure 4**a,b, ARPES measurements were carried out on MBE-grown 1-UC (bilayer) Bi_2O_2Se films with photons of 21.2 eV from a helium-discharging lamp. Figure 4c-i,ii shows the photoemission spectra intensity maps at the valance band maximum (VBM, or $E_F - 1.06$ eV) and VBM − 0.4 eV, respectively. We observe a warped square near the VBM, which splits with increased binding energy. Figure 4d presents the general high-symmetry band dispersions along $\overline{\Gamma}$–$\overline{X}$ and $\overline{X}$–$\overline{M}$, which is dominated by two hole-like bands α and β near VBM around $\overline{X}$ point. In the stacking plots of constant energy contours (Figure 4b), the evolution of this two hole-like bands at higher binding energy is clearly observed. By magnifying the spectra around $\overline{\Gamma}$ near the Fermi level, we observe weak intensity from the bottom of the conduction band, as shown in the inset of Figure 4d,e, indicating the existence of an indirect bandgap in Bi_2O_2Se. We do not observe any in-gap states such as the pinned impurity state throughout the whole 2D Brillouin zone, indicating high quality of MBE-grown 1-UC Bi_2O_2Se film.

In order to quantitatively extract the crucial indirect bandgap, we performed surface potassium dosing to raise the Fermi level of the system so that the conduction band minimum (CBM) can be accurately determined. Figure 4f-i) shows the band structure along $\overline{X}$–$\overline{\Gamma}$–$\overline{X}$ direction after potassium dosing, with the Fermi level raised about 100 meV compared with the pristine film shown in Figure 4e. The downward shift of the conduction band as shown in the inset of Figure 4f-i), enables us to acquire the details of the dispersion of the conduction band (the appended red curve). By fitting the dispersions around the band bottom with parabolic curve (the appended green curve), we can extract the in-plane ($k_x - k_y$) effective mass m^* of the conduction band, and m^* is estimated to be ≈0.15 m_0, with m_0 denoting the bare electron mass, which is lower than the values in typical semiconductors such as silicon[33] and MoS_2,[34] but slightly larger than the value in bulk Bi_2O_2Se. From the energy

 © 2019 WILEY-VCH Verlag GmbH & Co. KGaA, Weinheim

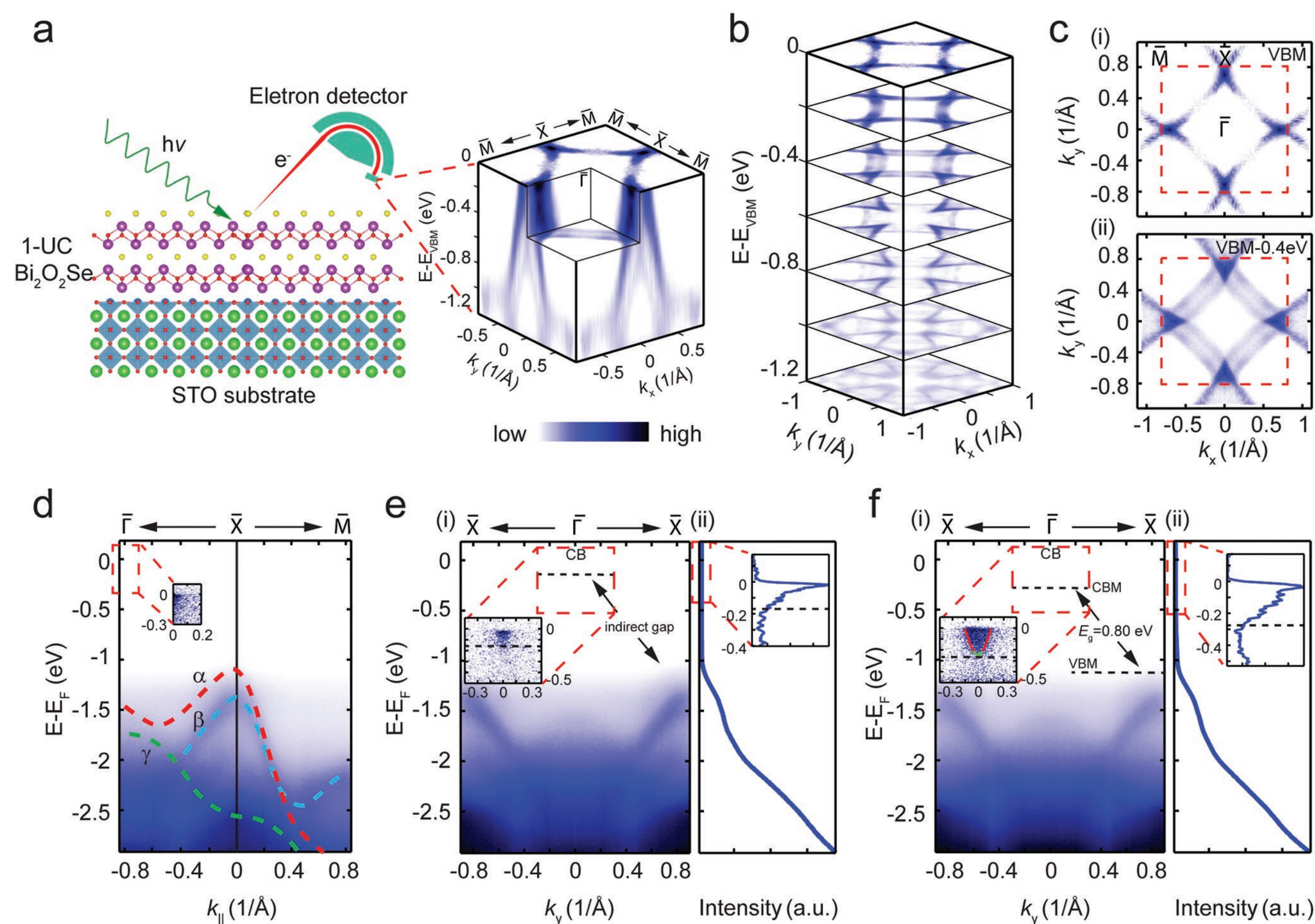

Figure 4. Electronic structures of MBE-grown 1-UC Bi_2O_2Se film. a) Schematic illustration of 1-UC thick Bi_2O_2Se film detected by ARPES with photons of 21.2 eV from a helium-discharging lamp. b) Stacking plots of constant energy contours in broad energy range showing the band structures evolution. c) Photoemission spectral intensity maps of the constant energy contours of bands at i) VBM and ii) VBM−0.4 eV, respectively. Integration over an energy window of 40 meV is included. Red dashed line is the projected Brillouin zone of the (001) surface of Bi_2O_2Se crystal, with high-symmetry points of Brillouin zone labeled. d) Band dispersions along $\overline{\Gamma}$–$\overline{M}$ of MBE-grown 1-UC thick Bi_2O_2Se film, with three main valance bands labelled by α, β, and γ, respectively. e,f) Band dispersions along $\overline{X}$–$\overline{\Gamma}$–$\overline{X}$ direction (i) and corresponding EDCs (ii) before (e) and after (f) surface potassium dosing, an indirect energy gap of ≈0.8 eV is clearly observed. Insets are zoom-in plots of conduction band and corresponding EDC with long-time integrated.

distribution curve (EDC) shown in Figure 4f-ii), we obtain the CBM at $E - E_F = -0.26$ eV and the VBM at $E - E_F = -1.06$ eV. Thus, the indirect bandgap equals ≈0.8 eV for the 1-UC Bi_2O_2Se film, in consistence with previous bulk measurements.[9]

In order to give a reasonable comparison between epitaxial thin film and bulk single crystal, we also conduct systematic ARPES measurements on bulk Bi_2O_2Se crystal using the same experiment setup (details can be found in the Supporting Information). The constant energy maps show nearly the same warped-square structures as on the MBE-grown 1-UC Bi_2O_2Se film. However, the spectrum is surprisingly more blurred than on the MBE film, suggesting that the crystal quality of our MBE film is even higher than the bulk material. As to the situation of band dispersions, the main α, β, and γ bands in bulk crystal are clearly observed, displaying similar dispersion shape with those in 1-UC film. However, despite nearly the same dispersion shape and intensity of α and β bands around $\overline{X}$ point, we find that the intensity of these three bands around $\overline{\Gamma}$ is strongly suppressed in the thin film. The different behaviors of the bands around $\overline{\Gamma}$ and $\overline{X}$ points strongly hint its origin of different orbital components. The thickness-dependent bands around $\overline{\Gamma}$ suggest it originates from delocalized out-of-plane orbitals, while thickness-independent bands around $\overline{X}$ indicate they are mainly formed by localized in-plane orbitals, which is quite consistent with the GGA calculations by Wu et al.,[9] the dominant orbitals of valance bands are Se p_z and Se $p_{x/y}$ around $\overline{\Gamma}$ and $\overline{X}$, respectively. We note that the overall observed bands shift upward about 40 meV in the bulk crystal, indicating the slight electron-doping in the as-grown thin film. The indirect bandgap of ≈0.74 eV in the bulk material is obtained from potassium dosing result, smaller than that in the thin film, which is qualitatively in good agreement with the tendency of thickness-dependent gap evolution evaluated by GGA calculations. We also extract the effective mass of about 0.10 m_0 of the conduction band, smaller than that of 0.15 m_0 in the thin film, which is quite consistent with the calculation results of 0.12 m_0 for bulk material while 0.16 m_0 for bilayer film by Wu et al.,[9] the dominant orbitals of valance bands are Se p_z and Se $p_{x/y}$

© 2019 WILEY-VCH Verlag GmbH & Co. KGaA, Weinheim

15214095, 2019, 39, Downloaded from https://onlinelibrary.wiley.com/doi/10.1002/adma.201901964 by Zhejiang University, Wiley Online Library on [04/09/2023]. See the Terms and Conditions (https://onlinelibrary.wiley.com/terms-and-conditions) on Wiley Online Library for rules of use; OA articles are governed by the applicable Creative Commons License

around $\overline{\Gamma}$ and $\overline{X}$, respectively. We note that the overall observed bands shift upward about 40 meV in the bulk crystal, indicating the slight electron-doping in the as-grown thin film. The indirect bandgap of ≈0.74 eV in the bulk material is obtained from potassium dosing result, smaller than that in the thin film, which is qualitatively in good agreement with the tendency of thickness-dependent gap evolution evaluated by GGA calculations. We also extract the effective mass of about 0.10 m_0 of the conduction band, smaller than that of 0.15 m_0 in the thin film, which is quite consistent with the calculation results of 0.12 m_0 for bulk material while 0.16 m_0 for bilayer film by Wu et al.[9] The GGA calculations[9] point out that the bottom of conduction band is dominated by out-of-plane Bi p_z orbital, while decreasing sample thickness, the band bottom is gradually contributed by in-plane Bi p_x and p_y orbitals. Despite this orbitals evolution behavior from bulk sample down to monolayer thin film limit, the moderate bandgap and small effective mass retain well in the high-quality ultrathin film, indicating the weak quantum size effect in Bi_2O_2Se, which may originate from the unique non-neutral layered structure of Bi_2O_2Se crystal.[15]

In conclusion, we have demonstrated the MBE-growth of atomically thin Bi_2O_2Se films down to monolayer by co-evaporating Bi and Se precursors in oxygen atmosphere. With optimized conditions, the growth adopts a 2D growth mode and precise thickness control has been achieved. Besides, the MBE-grown high-quality Bi_2O_2Se on STO shows an atomically sharp interface and atom-to-atom alignment. Using ARPES, the electronic structures of MBE-grown 1-UC (bilayer) Bi_2O_2Se films were successfully observed, displaying low effective mass of 0.15 m_0 and very slightly bandgap enlarging compared to bulk one.

Additionally, in view of practical device applications, it would be better to grow atomically thin Bi_2O_2Se film on insulating $SrTiO_3$ substrate (as shown in Figure S5, Supporting Information), whose heating mode should be changed and precise substrate treatments are needed to avoid the undesirable formation of oxygen vacancies under vacuum heating. Besides, theoretical calculation results predict that the thermoelectric performance can be significantly improved by application of tensile strain on monolayer Bi_2O_2Se.[35] Theoretically, the tensile strain in MBE-grown Bi_2O_2Se film can easily be tuned through changing the epitaxial substrate from $SrTiO_3$ to piezoelectric PMN-PT,[36] whose lattice parameter can be gradually tuned by applying an external voltage bias. These topics need further research in the future.

Supporting Information

Supporting Information is available from the Wiley Online Library or from the author.

Acknowledgements

Y.L. and Y.J.C. contributed equally to this work. The authors acknowledge financial support from the National Natural Science Foundation of China (21733001, 21525310, and 51672007), the National Basic Research Program of China (2016YFA0200101), and China Postdoctoral Science Foundation Funded Project. The authors gratefully acknowledge Electron Microscopy Laboratory in Peking University for the use of Cs corrected electron microscope. H.L.P., J.D.G., H.T.Y., and Y.L. conceived the experiments. Y.L., C.W.T., and X.F.X. carried out the synthesis and structural characterizations. Y.W.S. performed the cross-sectional TEM under direction of P.G. Y.J.C., L.X.Y., and Y.L.C. performed the ARPES characterizations. H.L.P., Y.L., Y.J.C., J.X.W., and S.P.X. wrote the manuscript. The whole work was supervised by H.L.P. and J.D.G. All authors discussed the results and commented on the manuscript.

Conflict of Interest

The authors declare no conflict of interest.

Keywords

2D materials, Bi_2O_2Se, molecular beam epitaxy, oxychalcogenides, ultrathin films

Received: March 28, 2019
Revised: July 25, 2019
Published online: August 7, 2019

[1] M. Chhowalla, H. S. Shin, G. Eda, L. J. Li, K. P. Loh, H. Zhang, *Nat. Chem.* **2013**, *5*, 263.
[2] Y. Liu, X. D. Duan, Y. Huang, X. F. Duan, *Chem. Soc. Rev.* **2018**, *47*, 6388.
[3] Q. Y. Wang, Z. Li, W. H. Zhang, Z. C. Zhang, J. S. Zhang, W. Li, H. Ding, Y. B. Ou, P. Deng, K. Chang, J. Wen, C. L. Song, K. He, J. F. Jia, S. H. Ji, Y. Y. Wang, L. L. Wang, X. Chen, X. C. Ma, Q. K. Xue, *Chin. Phys. Lett.* **2012**, *29*, 037402.
[4] S. Y. Zhang, J. Q. Guan, Y. Wang, T. Berlijn, S. Johnston, X. Jia, B. Liu, Q. Zhu, Q. C. An, S. W. Xue, Y. W. Cao, F. Yang, W. H. Wang, J. D. Zhang, E. W. Plummer, X. T. Zhu, J. D. Guo, *Phys. Rev. B* **2018**, *97*, 035408.
[5] H. L. Peng, K. J. Lai, D. S. Kong, S. Meister, Y. L. Chen, X. L. Qi, S. C. Zhang, Z. X. Shen, Y. Cui, *Nat. Mater.* **2010**, *9*, 225.
[6] H. J. Zhang, C. X. Liu, X. L. Qi, X. Dai, Z. Fang, S. C. Zhang, *Nat. Phys.* **2009**, *5*, 438.
[7] A. Ohtomo, H. Y. Hwang, *Nature* **2004**, *427*, 423.
[8] N. Reyren, S. Thiel, A. D. Caviglia, L. F. Kourkoutis, G. Hammerl, C. Richter, C. W. Schneider, T. Kopp, A. S. Ruetschi, D. Jaccard, M. Gabay, D. A. Muller, J. M. Triscone, J. Mannhart, *Science* **2007**, *317*, 1196.
[9] J. X. Wu, H. T. Yuan, M. M. Meng, C. Chen, Y. Sun, Z. Y. Chen, W. H. Dang, C. W. Tan, Y. J. Liu, J. B. Yin, Y. B. Zhou, S. Y. Huang, H. Q. Xu, Y. Cui, H. Y. Hwang, Z. F. Liu, Y. L. Chen, B. H. Yan, H. L. Peng, *Nat. Nanotechnol.* **2017**, *12*, 530.
[10] L. D. Zhao, J. Q. He, D. Berardan, Y. H. Lin, J. F. Li, C. W. Nan, N. Dragoe, *Energy Environ. Sci.* **2014**, *7*, 2900.
[11] J. L. Lan, B. Zhan, Y. C. Liu, B. Zheng, Y. Liu, Y. H. Lin, C. W. Nan, *Appl. Phys. Lett.* **2013**, *102*, 123905.
[12] X. Tan, J. L. Lan, Y. C. Liu, G. K. Ren, C. C. Zeng, Y. H. Lin, C. W. Nan, *J. Electroceram.* **2016**, *37*, 66.
[13] M. H. Wu, X. C. Zeng, *Nano Lett.* **2017**, *17*, 6309.
[14] A. Krzton-Maziopa, Z. Guguchia, E. Pomjakushina, V. Pomjakushin, R. Khasanov, H. Luetkens, P. K. Biswas, A. Amato, H. Keller, K. Conder, *J. Phys.: Condens. Matter* **2014**, *26*, 215702.
[15] J. X. Wu, C. W. Tan, Z. J. Tan, Y. J. Liu, J. B. Yin, W. H. Dang, M. Z. Wang, H. L. Peng, *Nano Lett.* **2017**, *17*, 3021.
[16] J. X. Wu, Y. J. Liu, Z. J. Tan, C. W. Tan, J. B. Yin, T. R. Li, T. Tu, H. L. Peng, *Adv. Mater.* **2017**, *29*, 1704060.
[17] C. Chen, M. X. Wang, J. X. Wu, H. X. Fu, H. F. Yang, Z. Tian, T. Tu, H. Peng, Y. Sun, X. Xu, J. Jiang, N. B. M. Schroter, Y. W. Li, D. Pei,

 © 2019 WILEY-VCH Verlag GmbH & Co. KGaA, Weinheim

15214095, 2019, 39, Downloaded from https://onlinelibrary.wiley.com/doi/10.1002/adma.201901964 by Zhejiang University, Wiley Online Library on [04/09/2023]. See the Terms and Conditions (https://onlinelibrary.wiley.com/terms-and-conditions) on Wiley Online Library for rules of use; OA articles are governed by the applicable Creative Commons License

S. Liu, S. A. Ekahana, H. T. Yuan, J. M. Xue, G. Li, J. F. Jia, Z. K. Liu, B. H. Yan, H. L. Peng, Y. L. Chen, *Sci. Adv.* **2018**, *4*, eaat8355.
[18] J. B. Yin, Z. J. Tan, H. Hong, J. X. Wu, H. T. Yuan, Y. J. Liu, C. Chen, C. W. Tan, F. R. Yao, T. R. Li, Y. L. Chen, Z. F. Liu, K. H. Liu, H. L. Peng, *Nat. Commun.* **2018**, *9*, 3311.
[19] H. X. Fu, J. X. Wu, H. L. Peng, B. H. Yan, *Phys. Rev. B* **2018**, *97*, 241203.
[20] J. X. Wu, C. G. Qiu, H. X. Fu, S. L. Chen, C. C. Zhang, Z. P. Dou, C. W. Tan, T. Tu, T. R. Li, Y. C. Zhang, Z. Y. Zhang, L. M. Peng, P. Gao, B. H. Yan, H. L. Peng, *Nano Lett.* **2019**, *19*, 197.
[21] C. W. Tan, M. Tang, J. X. Wu, Y. N. Liu, T. R. Li, Y. Liang, B. Deng, Z. J. Tan, T. Tu, Y. C. Zhang, C. Liu, J. H. Chen, Y. Wang, H. L. Peng, *Nano Lett.* **2019**, *19*, 2148.
[22] R. G. Quhe, J. C. Liu, J. X. Wu, J. Yang, Y. Y. Wang, Q. H. Li, T. R. Li, Y. Guo, J. B. Yang, H. L. Peng, M. Lei, J. Lu, *Nanoscale* **2019**, *11*, 532.
[23] U. Khan, Y. T. Luo, L. Tang, C. J. Teng, J. M. Liu, B. L. Liu, H. M. Cheng, *Adv. Funct. Mater.* **2019**, *29*, 1807979.
[24] J. Li, Z. X. Wang, Y. Wen, J. W. Chu, L. Yin, R. Q. Cheng, L. Lei, P. He, C. Jiang, L. P. Feng, J. He, *Adv. Funct. Mater.* **2018**, *28*, 1706437.
[25] Q. D. Fu, C. Zhu, X. X. Zhao, X. L. Wang, A. Chaturvedi, C. Zhu, X. W. Wang, Q. S. Zeng, J. D. Zhou, F. C. Liu, B. K. Tay, H. Zhang, S. J. Pennycook, Z. Liu, *Adv. Mater.* **2019**, *31*, 1804945.
[26] D. G. Schlom, L. Q. Chen, X. Q. Pan, A. Schmehl, M. A. Zurbuchen, *J. Am. Ceram. Soc.* **2008**, *91*, 2429.
[27] Y. Liang, W. T. Li, S. Y. Zhang, C. J. Lin, C. Li, Y. Yao, Y. Q. Li, H. Yang, J. D. Guo, *Sci. Rep.* **2015**, *5*, 10634.
[28] Y. Y. Li, G. A. Wang, X. G. Zhu, M. H. Liu, C. Ye, X. Chen, Y. Y. Wang, K. He, L. L. Wang, X. C. Ma, H. J. Zhang, X. Dai, Z. Fang, X. C. Xie, Y. Liu, X. L. Qi, J. F. Jia, S. C. Zhang, Q. K. Xue, *Adv. Mater.* **2010**, *22*, 4002.
[29] Y. Zhang, K. He, C. Z. Chang, C. L. Song, L. L. Wang, X. Chen, J. F. Jia, Z. Fang, X. Dai, W. Y. Shan, S. Q. Shen, Q. Niu, X. L. Qi, S. C. Zhang, X. C. Ma, Q. K. Xue, *Nat. Phys.* **2010**, *6*, 584.
[30] G. H. Zhang, H. J. Qin, J. Chen, X. Y. He, L. Lu, Y. Q. Li, K. H. Wu, *Adv. Funct. Mater.* **2011**, *21*, 2351.
[31] J. F. Ihlefeld, A. Kumar, V. Gopalan, D. G. Schlom, Y. B. Chen, X. Q. Pan, T. Heeg, J. Schubert, X. Ke, P. Schiffer, J. Orenstein, L. W. Martin, Y. H. Chu, R. Ramesh, *Appl. Phys. Lett.* **2007**, *91*, 071922.
[32] S. Stoughton, M. Showak, Q. Mao, P. Koirala, D. A. Hillsberry, S. Sallis, L. F. Kourkoutis, K. Nguyen, L. F. J. Piper, D. A. Tenne, N. J. Podraza, D. A. Muller, C. Adamo, D. G. Schlom, *APL Mater.* **2013**, *1*, 042112.
[33] L. E. Ramos, L. K. Teles, L. M. R. Scolfaro, J. L. P. Castineira, A. L. Rosa, J. R. Leite, *Phys. Rev. B* **2001**, *63*, 165210.
[34] W. X. Zhang, Z. S. Huang, W. L. Zhang, Y. R. Li, *Nano Res.* **2014**, *7*, 1731.
[35] N. Wang, M. Li, H. Xiao, H. Gong, Z. Liu, X. Zu, L. Qiao, *Phys. Chem. Chem. Phys.* **2019**, *21*, 15097.
[36] A. Herklotz, J. D. Plumhof, A. Rastelli, O. G. Schmidt, L. Schultz, K. Dorr, *J. Appl. Phys.* **2010**, *108*, 094101.

© 2019 WILEY-VCH Verlag GmbH & Co. KGaA, Weinheim

15214095, 2019, 39, Downloaded from https://onlinelibrary.wiley.com/doi/10.1002/adma.201901964 by Zhejiang University, Wiley Online Library on [04/09/2023]. See the Terms and Conditions (https://onlinelibrary.wiley.com/terms-and-conditions) on Wiley Online Library for rules of use; OA articles are governed by the applicable Creative Commons License